

8.3 Microscopy and surface analytics

T. Yokosawa, K. Hinz, W. Tobie, M. Plaschke, M. Brandauer, E. Soballa, D. Schild, H. Geckeis

In co-operation with:

C.-O. Krauß^a, A. Heneka^a, S. Gentes^a

^a Department of Deconstruction and Decommissioning of Conventional and Nuclear Buildings, Institute for Technology and Management in Construction (TMB), Karlsruhe Institute of Technology (KIT)

Introduction

Nuclear waste forms and brines at a deep underground repository may contain borate. In case water ingress and failure of the nuclear waste containers, the chemical state of released radionuclides affects their ability to migrate. Secondary phase formation can attenuate migration of highly mobile Np(V). New solids of Np-borate formed in diluted brines are analyzed by electron microscopy and spectroscopy.

Oxidation of spent nuclear fuel towards U_3O_8 in case of cladding failure during intermediate long-term storage is accompanied by an increase in volume of 31% which disintegrates pellets. The initial oxidation of an UO_2 pellet surface at the atmosphere is studied by angle-dependent XPS.

Interaction of abrasive particles with steel during water abrasive suspension cutting is characterized by SEM-EDX. This cutting technique is beneficial if applied to activated components with internal stress such as in the deconstruction of nuclear reactor pressure vessels and internals.

Investigation of Neptunium-borate by SEM, XPS, and TEM

In this study, the interaction of highly mobile Np(V) with borate in diluted NaCl and $MgCl_2$ solutions was analyzed by solubility experiments with solid amorphous NpO_2OH . Np(V)-borate complexes have a minor impact on the solubility of Np(V) at near-neutral to weakly alkaline pH. In dilute NaCl (0.1 M) or $MgCl_2$ (0.25 M) solutions with 0.16 M B and $pH_m < 9$, however, the Np(V) solubility is lowered by 3 to 4 orders of magnitude after 270 days of experiment. The color of the solid phase changed from greenish to light grey [1]. The solids were washed with ethanol prior to characterization by XRD, XPS, SEM-EDX, and TEM.

SEM images of the newly formed Np(V)-borate sol-

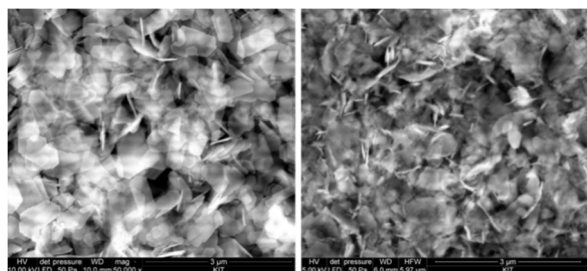


Fig. 1: SEM images of Np(V)-borate phases formed in solutions of 0.1 M NaCl (left) or 0.25 M $MgCl_2$ (right).

id phases recorded by a FEI Quanta 650 FEG instrument are shown in Fig. 1. The sample equilibrated in 0.1 M NaCl is composed of thin (~20 nm) hexagonal platelets with a size of about 500 nm, whereas the platelets of the sample equilibrated in 0.25 M $MgCl_2$ appear less crystallized. SEM-EDX of the Np(V) secondary phases detects O, Na, Mg, and Np, XPS

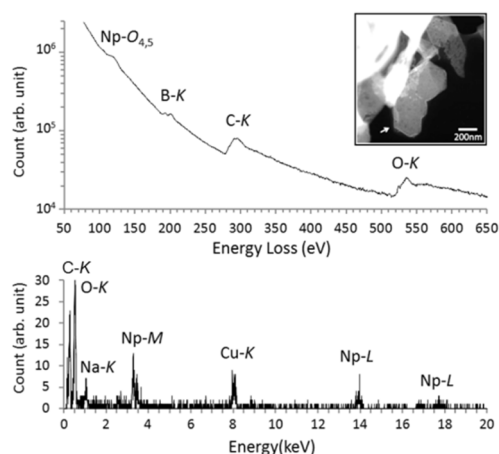


Fig. 2: EELS (top) and TEM-EDX (bottom) of Np(V)-borate phase formed in 0.1 M NaCl solution.

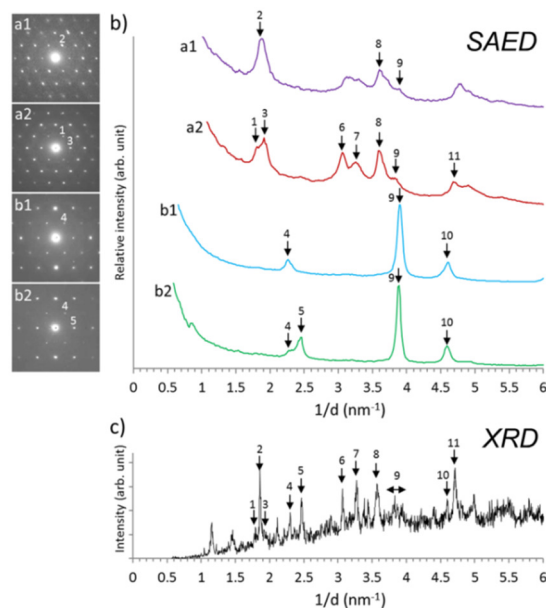


Fig. 3: SAED patterns of various particles of Np(V)-borate formed in 0.1 M NaCl solution. Diffractograms obtained by rotational averaging of the SAED patterns are compared to powder XRD data.

additionally shows presence of B, whereas Cl is not detected. The EDX detector was not able to detect boron. Atomic concentrations are determined by XPS survey spectra. Narrow scans of elemental lines indicate Np(V) and a single B species. The stoichiometry of the solid phases deduced from XPS data is supposed to be neptunyl-pentaborate – $\text{NpO}_2[\text{B}_5\text{O}_6(\text{OH})_4] \cdot 2\text{NaOH}$ in case of NaCl solution and $(\text{NpO}_2)_2[\text{B}_5\text{O}_6(\text{OH})_4]_2 \cdot 3\text{Mg}(\text{OH})_2$ in case of MgCl_2 solution, respectively.

TEM measurements are performed by employing a FEI Tecnai G2 F20 X-TWIN operated at 200 kV, located at IAM-WBM-FML (KIT). EELS and EDX spectra (Fig. 2) of the sample equilibrated in 0.1 M NaCl show the presence of Np, B, O, and Na, consistent with the result obtained by XPS. Since powder XRD diffractograms obtained for the newly formed solid phase with crystalline character gave no positive match with any of the existing borate entries in the JCPDS database, selected area electron diffraction (SAED) was applied (Fig. 3). Comparing the SAED radial profiles to the XRD profile, diffraction peaks indicated by 1, 2,... and 11 observed in the radial profiles and in the XRD profile show a good match at the peak positions, although there are some diffraction peaks in the XRD profile which were not observed by SAED in this study. Thus, it was revealed by SAED that the sample of 0.1 M NaCl contains several (at least four) phases which show different SAED patterns from each other, causing difficulty in performing the phase identification by XRD.

Oxidation of UO_2 pellet exposed to atmosphere

Exposure of UO_2 to the atmosphere results in fast formation of UO_{2+x} ($x < 0.25$) at the surface via diffusion of oxygen. U_4O_9 is formed which transforms to U_3O_7 during ongoing oxidation. Subsequent nucleation and growth yields U_3O_8 which is the most abundant form of uranium found in nature. Further oxidation to UO_3 is very slow. The oxidation from UO_2 to U_3O_8 is accompanied by an increase in volume by 31% which will disintegrate UO_2 pellets [2]. There is a still ongoing discussion about how this oxidation proceeds, either via U(IV,VI)-oxides or if U(V) is involved, e.g., U_4O_9 is represented by $(\text{UO}_2)_3 \cdot \text{UO}_3$ or $(\text{UO}_2)_2 \cdot \text{U}_2\text{O}_5$. In nature, wyartite $\text{CaU}^{(\text{V})}(\text{UO}_2)_2\text{O}_4(\text{CO}_3)(\text{OH}) \cdot 7\text{H}_2\text{O}$, which is a natural alteration product of uraninite, was the first mineral identified to contain U(V) [3]. The presence of U(V) in U_3O_8 was predicted theoretically [4]. U(V) in U_4O_9 and U_3O_8 ($\text{U}_2\text{O}_5 \cdot \text{UO}_3$) was observed by use of HERFD-XANES [5].

In this study, an ULVAC-PHI VersaProbe II X-ray photoelectron spectrometer was used for analyses of the outermost surface of a polished sintered UO_2 pellet exposed to the atmosphere during 15 months at room temperature after H_2 annealing. Angle-dependent XPS (ADXPS) was applied by recording narrow scans of elemental lines at various angles between pellet surface normal and analyzer axis in order to probe differ-

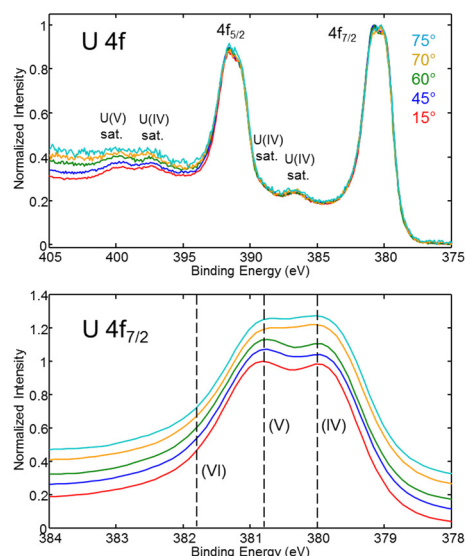


Fig. 4: ADXPS narrow scans of U 4f elemental lines of oxidized UO_2 pellet recorded at various angles between surface normal and analyzer. Enhanced view of U 4f_{7/2} shows the result of deconvolution (stack plot). Binding energies typical for the valence states of U are indicated.

ent depths. Monochromatic $\text{Al K}\alpha$ X-ray excitation and pass energy of the analyzer of 23.5 eV was used. The acceptance angle into the analyzer was 0.1 sr. U 4f and C 1s spectra are similar at all measured angles, whereas O 1s spectra differ (Figs. 4, 5). The U 4f elemental lines are composed of two main components of similar intensity. In Figure 4 the U 4f_{7/2} lines are additionally deconvolved applying the maximum entropy method [6] to a virtual pass energy of 2.95 eV of the analyzer by (PHI-ULVAC software MultiPak Ver.7.1). The U 4f_{7/2} binding energies (380.0 eV and 380.8 eV) and binding energy separations between main line and associated shake-up satellite (6.6 eV and

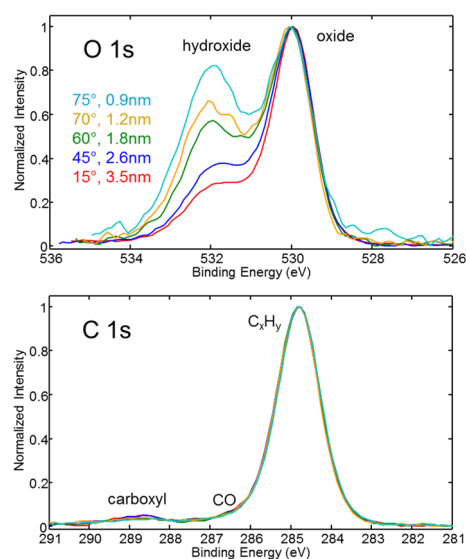


Fig. 5: ADXPS narrow scans of O 1s and C 1s elemental lines of oxidized UO_2 pellet recorded at different angles between surface normal and analyzer. Depths of information (95% of signal) are calculated for different angles.

8.1 eV, respectively) are characteristic for U(IV) and U(V) [7]. Similar abundances of U(IV) and U(V) point to the existence of U_4O_9 at the pellet surface. The portion of U(VI) is less than 7% as revealed by a curve-fit. O 1s spectra show two components, the binding energy of the component at 530.0 eV is characteristic for oxide; the component at 532.0 eV is assigned to hydroxide. According to analyses of uranium minerals [8] the binding energy of the hydroxide portion is typical for OH in the equatorial plane of uranyl polyhedrons.

Probing different depths by ADXPS shows enhanced abundance of hydroxide at the outermost surface of the pellet. A homogeneous layer model consisting of an adventitious hydrocarbon layer at the outermost surface, a hydroxylated layer, and U_4O_9 beneath is employed to estimate the extent of hydroxide formation. Since the adventitious hydrocarbon layer does not contain significant amounts of oxygen (only in traces of carboxylic and COH groups), Strohmeier's equation [9] and C2 equation for electron effective attenuation lengths [10] are employed for calculation of the thickness of hydroxylated layer by use of curve-fits to O 1s spectra. The thickness of the hydroxylated layer is about 0.5 nm, calculated at 45° between surface normal and analyzer axis. Since the results for the thickness vary at various angles by about 10%, a gradient of the hydroxide concentration is likely, similar to results by Marchetti [11], who immersed UO_2 in ^{18}O labelled water and applied SIMS depth profiling. The thickness of the adventitious hydrocarbon layer is calculated to 0.8 nm by comparison of the C 1s intensity with that of low density-polyethylene as a model substance for adventitious hydrocarbon.

The result of this study shows that (a) valence state identification of uranium is feasible by XPS with monochromatic X-ray excitation, (b) a hydroxylated layer with U(IV,V)-oxide U_4O_9 beneath is formed at ambient conditions, (c) the hydroxylated layer is not carbonated at the experimental conditions applied.

MASK project: SEM analyses

The objective of the BMBF project MASK is the magnet separation of granular mixtures of waterjet cutting to minimize secondary waste in the decommissioning of nuclear facilities.

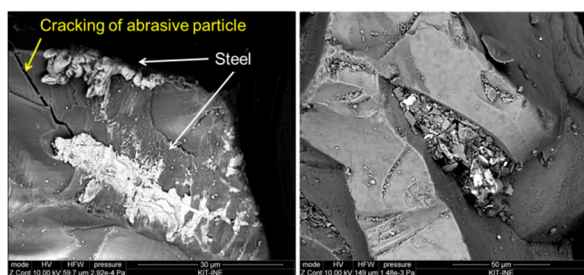


Fig. 6: Backscattered electron images. Left image: edge of an abrasive particle (grey) with steel adherence (light) and crack formation, horizontal field width of image: 60 μm . Right image: filling of void at an abrasive particle; horizontal field width of image: 149 μm .

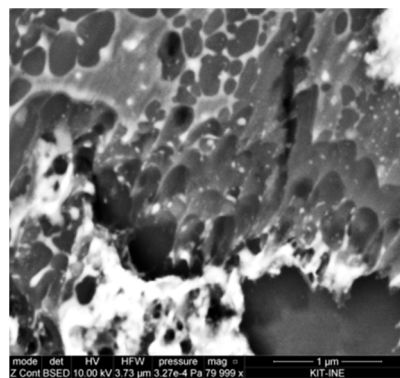


Fig. 7: Backscattered electron image of steel adherence to an abrasive particle showing evidence of solidified melt of steel and abrasive material. Horizontal field width of image: 3.73 μm .

The dissection of the reactor pressure vessel and internals may be performed by cutting with a high-pressure waterjet with admixture of abrasive grains. To reduce the radioactivity of the used solid material which is composed of about 98 wt% abrasive grains and 2 wt% radioactive steel cuttings, magnet separation is applied to the suspension. SEM imaging of separated abrasive grains show in some cases steel adherences and void filling (Fig. 6). The steel adherences originate from impact of abrasive particles onto steel. In addition, fractures occur in the vicinity of impact areas at abrasive grains causing fragmentation. Closer analyses of the steel adherences show signs of solidified melts of steel and abrasive material (Fig. 7). The abrasive grains are sharp-edged almandine, $Fe_3Al_2(SiO_4)_3$, a mineral with a density of 4.2 g/cm^3 , hardness of 7.5 - 8.5 on Mohs scale, and melting point of (1250 - 1315) $^\circ\text{C}$. Stainless steel has a density of 8 g/cm^3 and a melting point of (1325 - 1530) $^\circ\text{C}$ depending on the specific alloy. The velocity of the waterjet is about 580 m/s, a typical abrasive grain has thus a kinetic energy of ~ 3 mJ. During impact of an abrasive grain onto steel the kinetic energy is dissipated within the contact time of 1 to 3 ns. Radiative heat transfer proportional to T^4 limits the temperature rise but it is still high enough to melt almandine and steel. However, the images indicate that intermixing of the materials during the melting process does not take place. Presently, the adherences of steel to abrasive grains limit the magnetic separation process and an additional treatment step is needed to improve the separation grade.

References

- [1] Hinz, K., *PhD thesis*, Karlsruhe Institute of Technology (2015).
- [2] McEachern, R.J. et al., *J. Nucl. Mat.* **254**, 87-121 (1998).
- [3] Burns, P.C., et al., *Am. Mineral.* **84**, 1456-1460 (1999).
- [4] Yun, Y., et al., *Phys. Rev. B* **83**, 075109 (2011).
- [5] Kvashnina, K.O., et al., *Phys. Rev. Lett.* **111**, 253002 (2013).

- [6] Jansson, P.A. (ed.), *Deconvolution of Images and Spectra*. Academic Press, London (1997).
- [7] Ilton, E.S., et al., *Surf. Interface Anal.* **43**, 1549-1560 (2011).
- [8] Schindler, M., et al., *Geochim. Cosmochim. Ac.* **73**, 2488-2509 (2009).
- [9] Strohmeier, B.R., *Surf. Interface Anal.* **15**, 51-56 (1990).
- [10] Cumpson, P.J., et al., *Surf. Interface Anal.* **25**, 430-446 (1997).
- [11] Marchetti, I., *PhD thesis*, Ruprechts Karls University Heidelberg, 61 (2013).